SURFACE SCIENCE SPECTRA

Fe_2O_3-WO_3 and Fe_2O_3-CuO nanoheterostructures by XPS

Cite as: Surf. Sci. Spectra **28**, 024003 (2021); https://doi.org/10.1116/6.0001252
Submitted: 01 July 2021 • Accepted: 29 September 2021 • Published Online: 18 October 2021

Chiara Maccato, Lorenzo Bigiani, Davide Barreca, et al.

SSS SURFACE SCIENCE SPECTRA

ARTICLE

avs.scitation.org/journal/sss

Fe_2O_3-WO_3 and Fe_2O_3-CuO nanoheterostructures by XPS

Cite as: Surf. Sci. Spectra **28**, 024003 (2021); doi: 10.1116/6.0001252
Submitted: 1 July 2021 · Accepted: 29 September 2021 ·
Published Online: 18 October 2021

Chiara Maccato,[1] Lorenzo Bigiani,[1] Davide Barreca,[2,a)] and Alberto Gasparotto[1]

AFFILIATIONS

[1]Department of Chemical Sciences, Padova University and INSTM, 35131 Padova, Italy
[2]CNR-ICMATE and INSTM, Department of Chemical Sciences, Padova University, 35131 Padova, Italy

[a)]**Author to whom correspondence should be addressed:** davide.barreca@unipd.it

ABSTRACT

The detrimental effects of gaseous nitrogen oxides (NO_x, with x = 1 and 2) on both human health and the environment have triggered efforts aimed at the development of solar-activated photocatalysts for their efficient removal. In this regard, Fe_2O_3-WO_3 and Fe_2O_3-CuO nanoheterostructures were prepared by a two-step vapor phase route. In particular, chemical vapor deposition (CVD) of β-Fe_2O_3, a scarcely investigated iron(III) oxide polymorph, was followed by radio frequency-sputtering of WO_3 or CuO under mild conditions. The adopted strategy enabled the obtainment of nanoheterostructures with a peculiar pyramidal morphology and a uniform dispersion of CuO or WO_3 onto the pristine iron(III) oxide. In this work, the chemical composition of the target systems was investigated by means of x-ray photoelectron and x-ray excited-Auger electron spectroscopies. In addition to the identification of elemental chemical states, the reported results confirmed the formation of pure and O-deficient systems, in which the direct interplay between the single components opens the door to air purification using the developed systems as photocatalysts.

Key words: Fe_2O_3, WO_3, CuO, CVD, RF-sputtering, x-ray photoelectron spectroscopy

Accession #: 01696 and 01697
Technique: XPS and XE-AES
Host Material: Fe_2O_3-WO_3 and Fe_2O_3-CuO
Instrument: Perkin-Elmer Physical Electronics, Inc. 5600ci
Major Elements in Spectra: C, O, Fe, W, and Cu
Minor Elements in Spectra: None
Published Spectra: 11
Spectra in Electronic Record: 11
Spectral Category: Comparison

INTRODUCTION

The family of iron(III) oxides has received a great deal of interest for functional applications in heterogeneous photocatalysis due to the low cost, biocompatibility, and suitable bandgaps for visible light absorption (Refs. 1–6). These features are particularly attractive for solar-activated removal of NO_x (De-NO_x), especially in urban/industrial contexts (Refs. 2 and 7–9), which is very important for both environment and human health protection. So far, De-NO_x studies have been almost entirely focused on α-Fe_2O_3 (*hematite*), the most stable iron(III) oxide phase (Refs. 2 and 8–11). Nevertheless, the attractive characteristics of the other iron(III) oxide polymorphs, such as the least investigated and metastable β-Fe_2O_3 ($E_G \approx 1.9$ eV) (Refs. 1 and 11–14), pave the way to their successful exploitation as De-NO_x photocatalysts.

During the course of our studies on iron(III) oxide systems (Refs. 4 and 12–16), we reported the first De-NO_x performances of β-Fe_2O_3 nanomaterials (Ref. 11). Inspired by these results, we extended our investigation to β-Fe_2O_3 nanoheterostructures. These materials are known to suppress charge carrier recombination, which is a significant problem that limits the efficiency of iron oxide photocatalysts (Refs. 1, 2, 4, 9, 15, and 17). Among the possible Fe_2O_3 functionalization agents, WO_3 and CuO have several favorable features. In fact, both Fe_2O_3/WO_3 and Fe_2O_3/CuO interfaces offer tunable band edge energetics and enhanced charge carrier separation (Refs. 14 and 18–21). In addition, WO_3 is characterized by good photostability, positioning it as a possible protective agent for Fe_2O_3 surface functionalization, and possessing a

bandgap enabling Vis light absorption (Refs. 18, 19, and 22–24). The latter advantage is offered even by CuO ($E_G \approx 1.8$ eV), a stable, low-cost and nontoxic system with a favorable chemical reactivity (Refs. 13, 25, and 26).

On this basis, we have devoted our attention to the synthesis and characterization of Fe_2O_3-WO_3 and Fe_2O_3-CuO nanoheterostructures. In particular, Fe_2O_3 systems were deposited on Si(100) by CVD and subsequently subjected to radio frequency (RF) sputtering processes aimed at the controlled introduction of tungsten or copper oxides. A multitechnique investigation of material structure, morphology, and composition revealed the formation of nanoheterostructured systems, in which the single constituent oxides maintain their chemical identity. In particular, the present contribution is focused on a detailed XPS and XE-AES analysis of representative Fe_2O_3-WO_3 and Fe_2O_3-CuO systems. The results reported and discussed herein provide an important insight into the chemical states of the main elements by analyzing the principal core level and Auger signals (C 1s, O 1s, Fe 2p, W 4f, Cu 2p, and Cu LMM). In addition, the data revealed the occurrence of an electronic interplay between material components, which may be an important starting point to achieve an improved separation of photogenerated charge carriers in view of De-NO_x applications.

SPECIMEN DESCRIPTION (ACCESSION # 01696)

Host Material: Fe_2O_3-WO_3
CAS Registry #: Unknown
Host Material Characteristics: Homogeneous; solid; polycrystalline; semiconductor; composite; and thin film
Chemical Name: Iron (III) oxide–tungsten (VI) oxide
Source: Sample obtained by the CVD of Fe_2O_3 on Si(100) and the subsequent introduction of WO_3 by RF-sputtering
Host Composition: Fe, O, and W
Form: Supported nanocomposite thin film
Structure: The specimen x-ray diffraction (XRD) pattern presented signals at $2\theta = 23.2°$, 33.0°, 38.3°, 45.2°, and 49.4° related, respectively, to (211), (222), (400), (332), and (431) reflections from cubic β-Fe_2O_3 (*bixbyite*) (Ref. 27). The absence of signals from other iron(III) oxide polymorphs highlighted the formation of phase-pure systems. An analysis of the relative peak intensities in comparison to those of the powdered reference material indicated the absence of any appreciable preferential orientation. No diffraction signals attributable to W-containing phases or to mixed Fe-W-O ones were observed, a phenomenon due to their low overall amount and high dispersion (Refs. 13, 22, 23, and 28). The system morphology, analyzed by field emission-scanning electron microscopy (FE-SEM) and atomic force microscopy (AFM), was dominated by homogeneously distributed and well faceted pyramidal aggregates (average dimensions ≈500 nm). The high "root mean square" (RMS) roughness (≈120 nm) suggested a high surface area (Refs. 4 and 11), a promising result for light-induced charge transfer at the system surface (Refs. 9, 11, 16, and 29–31) for an improved material photoactivity.
History and Significance: CVD of Fe_2O_3 nanosystems was performed by means of a custom-built, horizontal CVD reactor equipped with a resistively heated metal susceptor and an external reservoir for precursor vaporization. $Fe(tfa)_2$•TMEDA (tfa = 1,1,1-trifluoro-2,4-pentanedionate; TMEDA = *N*,*N*,*N*′,*N*′-tetramethylethylenediamine) was chosen as iron molecular source and prepared through the reaction of $FeCl_2$•$4H_2O$ with Htfa and TMEDA in aqueous NaOH. Before deposition, *p*-type Si(100) substrates (MEMC®, Merano, Italy) were precleaned by immersion in isopropyl alcohol, dichloroethane, and final etching in an HF aqueous solution to remove the native SiO_2 layer. After a preliminary optimization of experimental conditions, growth processes were carried out using the following settings: substrate temperature = 500 °C; total pressure = 10.0 mbar; duration = 2 h; precursor vaporization temperature = 80 °C; and total oxygen flow rate = 200 standard cubic centimeters per minute (SCCM). Functionalization of as-grown Fe_2O_3 specimens was performed by RF-sputtering from Ar plasmas using a two-electrode custom-built apparatus (ν = 13.56 MHz), in which Si-supported Fe_2O_3 samples were mounted on the grounded electrode, and a tungsten oxide target (Neyco®; purity = 99.99%) on the RF one. The following experimental conditions were adopted: growth temperature = 60 °C; total pressure = 0.3 mbar; duration = 3 h; Ar flow rate = 10 SCCM; and RF-power = 20 W.
As Received Condition: As grown
Analyzed Region: Same as host material
***Ex Situ* Preparation/Mounting:** Specimen was mounted on a metallic sample holder and introduced into the instrument chamber through a fast entry lock system.
***In Situ* Preparation:** None
Charge Control: No flood gun was used.
Temp. During Analysis: 298 K
Pressure During Analysis: $<10^{-8}$ Pa
Preanalysis Beam Exposure: 200 s

SPECIMEN DESCRIPTION (ACCESSION # 01697)

Host Material: Fe_2O_3-CuO
CAS Registry #: Unknown
Host Material Characteristics: Homogeneous; solid; polycrystalline; semiconductor; composite; and thin film
Chemical Name: Iron (III) oxide–copper(II) oxide
Source: Sample obtained by the CVD of Fe_2O_3 on Si(100) and the subsequent introduction of CuO by RF-sputtering
Host Composition: Fe, O, and Cu
Form: Supported nanocomposite thin film
Structure: The sample XRD pattern was very similar to that of the previous specimen, and for the same reasons, no reflections related to copper-containing phases could be detected. Accordingly, FE-SEM and AFM analyses revealed no appreciable differences in the system morphology with respect to the case of Fe_2O_3-WO_3.
History and Significance: The growth of Fe_2O_3 on Si(100) substrates by CVD was performed using the same experimental settings already indicated for the previous accession. The subsequent functionalization with CuO was performed by RF-sputtering from a copper target (Alfa Aesar®; purity ≥ 99.95%) using the same experimental settings reported for WO_3, apart from the RF-power and process duration which were set at 5 W and 2 h, respectively.

As Received Condition: As grown
Analyzed Region: Same as host material
***Ex Situ* Preparation/Mounting:** Specimen was mounted on a metallic sample holder and introduced into the instrument chamber through a fast entry lock system.
***In Situ* Preparation:** None
Charge Control: No flood gun was used.
Temp. During Analysis: 298 K
Pressure During Analysis: $<10^{-8}$ Pa
Preanalysis Beam Exposure: 220 s

INSTRUMENT DESCRIPTION

Manufacturer and Model: Perkin-Elmer Physical Electronics, Inc. 5600ci
Analyzer Type: Spherical sector
Detector: Channeltron
Number of Detector Elements: 16

INSTRUMENT PARAMETERS COMMON TO ALL SPECTRA

Spectrometer

Analyzer Mode: Constant pass energy
Throughput ($T = E^N$): N = 0
Excitation Source Window: 1.5 μm Al window
Excitation Source: Al K_α
Source Energy: 1486.6 eV
Source Strength: 250 W
Source Beam Size: >25 000 × >25 000 μm^2
Signal Mode: Multichannel direct

Geometry

Incident Angle: 9°
Source-to-Analyzer Angle: 53.8°
Emission Angle: 45°
Specimen Azimuthal Angle: 0°
Acceptance Angle from Analyzer Axis: 0°
Analyzer Angular Acceptance Width: 14° × 14°

Ion Gun

Manufacturer and Model: PHI 04-303 A
Energy: 4000 eV
Current: 0.4 mA/cm^2
Current Measurement Method: Faraday cup
Sputtering Species: Ar^+
Spot Size (unrastered): 250 μm
Raster Size: 2000 × 2000 μm^2
Incident Angle: 40°
Polar Angle: 45°
Azimuthal Angle: 111°
Comment: Differentially pumped ion gun

DATA ANALYSIS METHOD

Energy Scale Correction: —
Recommended Energy Scale Shift: 0 eV for both samples
Peak Shape and Background Method: After a Shirley-type background subtraction (Ref. 32), peak positions and widths were obtained by a least-square fitting procedure using Gaussian/Lorentzian sum functions (% Lorentzian = 40%).
Quantitation Method: Atomic percentages (at. %) were determined by means of peak area integration using PHI V5.4A sensitivity factors.

ACKNOWLEDGMENTS

This work was financially supported by Padova University (DOR 2018–2020, P-DiSC No. 04BIRD2020-UNIPD EUREKA), INSTM Consortium (INSTM21PDBARMAC—ATENA, INSTM21PDGASPAROTTO—NANO^{MAT}), and AMGA Foundation (NYMPHEA project). M. Klotzsche, C. Incao, and L. Vanin (Department of Chemical Sciences, Padova University, Padova, Italy) are acknowledged for useful experimental support.

DATA AVAILABILITY

The data that support the findings of this study are available within the article and its supplementary material.

REFERENCES

[1]K. C. Christoforidis, T. Montini, E. Bontempi, S. Zafeiratos, J. J. D. Jaén, and P. Fornasiero, Appl. Catal. B **187**, 171 (2016).
[2]J. Balbuena, M. Cruz-Yusta, A. L. Cuevas, M. C. López-Escalante, F. Martín, A. Pastor, and L. Sánchez, RSC Adv. **6**, 92917 (2016).
[3]R. Cornell and U. Schwertmann, *The Iron Oxides: Structures, Properties, Reactions, Occurrences and Uses*, 2nd ed. (Wiley-VCH Verlag, Weinheim, 2003).
[4]G. Carraro, D. Barreca, D. Bekermann, T. Montini, A. Gasparotto, V. Gombac, C. Maccato, and P. Fornasiero, J. Nanosci. Nanotechnol. **13**, 4962 (2013).
[5]E. Alp, H. Eşgin, M. K. Kazmanlı, and A. Genç, Ceram. Int. **45**, 9174 (2019).
[6]R. Khurram, Z. Wang, and M. F. Ehsan, Environ. Sci. Pollut. Res. **28**, 17697 (2021).
[7]P. Zhang, Y. Huang, Y. Rao, M. Chen, X. Li, W. Ho, S. Lee, and J. Cao, Chem. Eng. J. **406**, 126910 (2021).
[8]R. Sugrañez, J. Balbuena, M. Cruz-Yusta, F. Martín, J. Morales, and L. Sánchez, Appl. Catal. B **165**, 529 (2015).
[9]J. Balbuena, M. Cruz-Yusta, A. Pastor, and L. Sánchez, J. Alloys Compd. **735**, 1553 (2018).
[10]J. Balbuena, M. Cruz-Yusta, A. L. Cuevas, F. Martín, A. Pastor, R. Romero, and L. Sánchez, J. Alloys Compd. **797**, 166 (2019).
[11]G. Carraro, R. Sugrañez, C. Maccato, A. Gasparotto, D. Barreca, C. Sada, M. Cruz-Yusta, and L. Sánchez, Thin Solid Films **564**, 121 (2014).
[12]G. Carraro, C. Maccato, E. Bontempi, A. Gasparotto, O. I. Lebedev, S. Turner, L. E. Depero, G. Van Tendeloo, and D. Barreca, Eur. J. Inorg. Chem. **2013**, 5454 (2013).
[13]G. Carraro, A. Gasparotto, C. Maccato, E. Bontempi, F. Bilo, D. Peeters, C. Sada, and D. Barreca, CrystEngComm **16**, 8710 (2014).
[14]G. Carraro *et al.*, Adv. Funct. Mater. **24**, 372 (2014).
[15]D. Barreca *et al.*, Int. J. Hydrogen Energy **38**, 14189 (2013).
[16]G. Carraro *et al.*, RSC Adv. **4**, 32174 (2014).
[17]L. Li *et al.*, Appl. Surf. Sci. **469**, 933 (2019).
[18]S. Bai, K. Zhang, J. Sun, R. Luo, D. Li, and A. Chen, CrystEngComm **16**, 3289 (2014).
[19]D. Bi and Y. Xu, J. Mol. Catal. A Chem. **367**, 103 (2013).
[20]A. Kanwal, S. Sajjad, S. A. K. Leghari, and Z. Yousaf, J. Phys. Chem. Solids **151**, 109899 (2021).
[21]S. Shekoohiyan, A. Rahmania, M. Chamack, G. Moussavi, O. Rahmanian, V. Alipour, and S. Giannakis, Sep. Purif. Technol. **242**, 116821 (2020).

[22]A. Gasparotto *et al.*, CrystEngComm **20**, 1282 (2018).
[23]D. Barreca, G. Carraro, A. Gasparotto, C. Maccato, T. Altantzis, C. Sada, K. Kaunisto, T.-P. Ruoko, and S. Bals, Adv. Mater. Interfaces **4**, 1700161 (2017).
[24]R. A. Senthil, A. Priya, J. Theerthagiri, A. Selvi, P. Nithyadharseni, and J. Madhavan, Ionics **24**, 3673 (2018).
[25]L. Zhu, H. Li, Z. Liu, P. Xia, Y. Xie, and D. Xiong, J. Phys. Chem. C **122**, 9531 (2018).
[26]D. Barreca, A. Gasparotto, C. Maccato, E. Tondello, O. I. Lebedev, and G. Van Tendeloo, Cryst. Growth Des. **9**, 2470 (2009).
[27]JCPDS Pattern No. 039-0238 (2000).
[28]L. Bigiani *et al.*, Appl. Catal. B **284**, 119684 (2021).
[29]J. Balbuena, J. M. Calatayud, M. Cruz-Yusta, P. Pardo, F. Martín, J. Alarcón, and L. Sánchez, Dalton Trans. **47**, 6590 (2018).
[30]A. Pastor, J. Balbuena, M. Cruz-Yusta, I. Pavlovic, and L. Sánchez, Chem. Eng. J. **368**, 659 (2019).
[31]R. Gusain, K. Gupta, P. Joshi, and O. P. Khatri, Adv. Colloid Interface Sci. **272**, 102009 (2019).
[32]D. A. Shirley, Phys. Rev. B **5**, 4709 (1972).
[33]D. Briggs and M. P. Seah, *Practical Surface Analysis: Auger and X-ray Photoelectron Spectroscopy*, 2nd ed. (Wiley, New York, 1990).
[34]J. F. Moulder, W. F. Stickle, P. E. Sobol, and K. D. Bomben, *Handbook of X-ray photoelectron spectroscopy* (Perkin Elmer Corporation, Eden Prairie, MN, 1992).
[35]L. Bigiani, D. Barreca, A. Gasparotto, and C. Maccato, Surf. Sci. Spectra **25**, 014003 (2018).
[36]X. Song, G. Qin, G. Cheng, W. Jiang, X. Chen, W. Dai, and X. Fu, Appl. Catal. B **284**, 119761 (2021).
[37]Y. Gao, N. Zhang, C. Wang, F. Zhao, and Y. Yu, ACS Appl. Energy Mater. **3**, 666 (2020).
[38]See the supplementary material at https://doi.org./10.1116/6.0001252 for Raw files.

SPECTRAL FEATURES TABLE

Spectrum ID #	Element/ Transition	Peak Energy (eV)	Peak Width FWHM (eV)	Peak Area (eV counts/s)[a]	Sensitivity Factor[b]	Concentration (at. %)	Peak Assignment
01696-02[a]	C 1s	284.8	1.8	6 297.9	0.296	16.5	Adventitious surface contamination
01696-02[a]	C 1s	286.3	2.0	3 304.4	0.296	8.6	C-O species from precursor residuals
01696-02[a]	C 1s	288.8	2.2	582.6	0.296	1.5	Adsorbed carbonates
01696-03[b]	O 1s	530.4	2.0	37 404.5	0.711	41.7	Lattice oxygen in Fe_2O_3 and WO_3
01696-03[b]	O 1s	531.7	2.3	11 110.9	0.711	12.4	Surface adsorbed—OH/carbonate groups
01696-04[c]	Fe 2p	…	…	38 478	2.957	10.7	Fe(III) in Fe_2O_3
01696-04	Fe $2p_{3/2}$	711.4	3.5	…	…	…	Fe(III) in Fe_2O_3
01696-04	Fe $2p_{1/2}$	724.9	3.5	…	…	…	Fe(III) in Fe_2O_3
01696-05[d]	W 4f	…	…	36 481	3.523	8.6	W(VI) in WO_3
01696-05	W $4f_{7/2}$	35.6	1.6	…	…	…	W(VI) in WO_3
01696-05	W $4f_{5/2}$	37.7	1.6	…	…	…	W(VI) in WO_3
01697-02[a]	C 1s	284.8	1.8	10 065.4	0.296	15.6	Adventitious surface contamination
01697-02[a]	C 1s	286.4	2.0	3 882.4	0.296	6.0	C-O species from precursor residuals
01697-02[a]	C 1s	288.7	2.2	1 396.2	0.296	2.2	Adsorbed carbonates
01697-03[b]	O 1s	529.9	1.7	54 268.4	0.711	33.8	Lattice oxygen in Fe_2O_3 and CuO
01697-03[b]	O 1s	531.6	2.1	30 338.1	0.711	19.0	Surface adsorbed—OH/carbonate groups
01697-04[c]	Fe 2p	…	…	11 4235	2.957	18.3	Fe(III) in Fe_2O_3
01697-04	Fe $2p_{3/2}$	711.1	3.6	…	…	…	Fe(III) in Fe_2O_3
01697-04	Fe $2p_{1/2}$	724.6	3.6	…	…	…	Fe(III) in Fe_2O_3
01697-05[e]	Cu 2p	…	…	57 081	5.321	5.1	Cu(II) in CuO
01697-05	Cu $2p_{3/2}$	934.0	4.0	…	…	…	Cu(II) in CuO
01697-05	Cu $2p_{1/2}$	953.7	4.0	…	…	…	Cu(II) in CuO
01697-06[f]	Cu LMM	917.3	…	…	…		Cu(II) in CuO

[a]The sensitivity factor refers to the whole C 1s signal.
[b]The sensitivity factor refers to the whole O 1s signal.
[c]The sensitivity factor, peak area, and concentration refer to the whole Fe 2p signal.
[d]The sensitivity factor, peak area, and concentration refer to the whole W 4f signal.
[e]The sensitivity factor, peak area, and concentration refer to the whole Cu 2p signal.
[f]Peak position in KE.

Footnote to Spectra 01696-02 and 01697-02: The C 1s photoelectron peaks could be fitted by three contributing bands. The main one, located at BE = 284.8 eV, was due to adventitious contamination arising from air exposure/sample manipulation. The second and third less intense ones (BE ≈ 286.3 and 288.7 eV) were ascribed to C-O species from precursor residuals and to the presence of surface adsorbed carbonates (Refs. 33–35). Nonetheless, the C 1s signal disappeared after 5 min of Ar^+ erosion, confirming the purity of the target specimens.

Footnote to Spectra 01696-03 and 01697-03: Two different components contributed to the O 1s photopeak. The main band (BE = 530.4 and 529.9 eV for Fe_2O_3-WO_3 and Fe_2O_3-CuO, respectively) was due to lattice oxygen (Refs. 4, 7, 8, 11, 12, 23, 25, and 34). The higher BE one (BE ≈ 531.6 eV) was attributed to surface carbonates/oxygen species chemisorbed on O defects (Refs. 28 and 34–38).

Footnote to Spectra 01696-04 and 01697-04: For both the target specimens, the Fe 2p signal shape and position were consistent with the presence of Fe_2O_3 as the sole iron oxide, in accordance with XRD results (see above). Nevertheless, a detailed data examination revealed that Fe $2p_{3/2}$ BE value underwent a little upward (711.4 eV) and downward (711.1 eV) shift for Fe_2O_3-WO_3 and Fe_2O_3-CuO specimens, respectively, in comparison to the value reported for pure iron(III) oxide (Refs. 2, 4, 8, 11, and 12). These variations can be related to the occurrence of electronic interactions between iron and copper/tungsten oxides in the obtained nanoheterostructures (Refs. 22, 23, and 37). More precisely, the presently reported data suggest that, at the Fe_2O_3/WO_3 interface, an electron transfer from Fe_2O_3 to WO_3 takes place, whereas in the case of Fe_2O_3/CuO the electron flow direction is reversed (see also comments to Accession Nos. 01696-05, 01697-05, and 01697-06). Similar phenomena are deemed to improve charge carrier separation in comparison to bare Fe_2O_3, resulting in an improved photocatalytic activity of the present Fe_2O_3-WO_3 and Fe_2O_3-CuO systems.

Footnote to Spectra 01696-05, 01697-05, and 01697-06: Consistent with the above discussed features, the W 4f and Cu 2p energy positions [BE(W$4f_{7/2}$) = 35.6 eV; BE(Cu$2p_{3/2}$) = 934.0 eV] were slightly lower and higher, respectively, than those reported for WO_3 (Refs. 22, 23, and 34) and CuO (Refs. 25, 26, and 34), supporting thus the aforementioned electron transfer processes. It is worth noting that the presence of CuO was in any case confirmed by the well-evident *shake-up* peaks in the Cu 2p signal (Ref. 33), as well as by the calculation of the copper Auger parameter α = BE(Cu$2p_{3/2}$) + KE(Cu LMM) (Refs. 13 and 33) which yielded a value of 1851.2 eV (Refs. 13 and 26).

ANALYZER CALIBRATION TABLE

Spectrum ID #	Element/ Transition	Peak Energy (eV)	Peak Width FWHM (eV)	Peak Area (eV × counts/s)	Sensitivity Factor	Concentration (at. %)	Peak Assignment
…[a]	Au $4f_{7/2}$	84.0	1.4	186403	…	…	Au(0)
…[a]	Cu $2p_{3/2}$	932.7	1.6	86973	…	…	Cu(0)

[a]The peak was acquired after Ar^+ erosion.

GUIDE TO FIGURES

Spectrum (Accession) #	Spectral Region	Voltage Shift	Multiplier	Baseline	Comment #
01696-01	Survey	0	1	0	…
01696-02	C 1s	0	1	0	…
01696-03	O 1s	0	1	0	…
01696-04	Fe 2p	0	1	0	…
01696-05	W 4f	0	1	0	…
01697-01	Survey	0	1	0	…
01697-02	C 1s	0	1	0	…
01697-03	O 1s	0	1	0	…
01697-04	Fe 2p	0	1	0	…
01697-05	Cu 2p	0	1	0	…
01697-06	Cu LMM	0	1	0	…

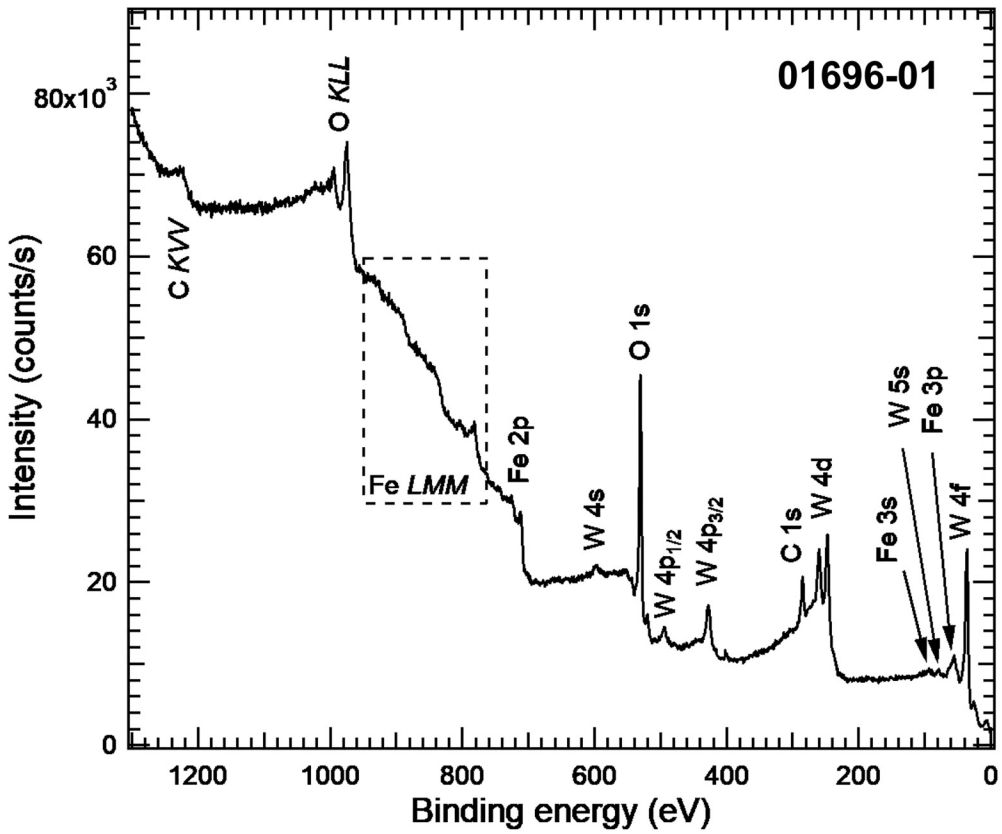

Accession #	01696-01
Host Material:	Fe_2O_3-WO_3
Technique:	XPS
Spectral Region:	Survey
Instrument:	Perkin-Elmer Physical Electronics, Inc. 5600ci
Excitation Source:	Al K_α
Source Energy:	1486.6 eV
Source Strength:	250 W
Source Size:	>25 × >25 mm^2
Analyzer Type:	Spherical sector analyzer
Incident Angle:	9°
Emission Angle:	45°
Analyzer Pass Energy:	187.85 eV
Analyzer Resolution:	1.9 eV
Total Signal Accumulation Time:	650.4 s
Total Elapsed Time:	715.4 s
Number of Scans:	20
Effective Detector Width:	1.9 eV

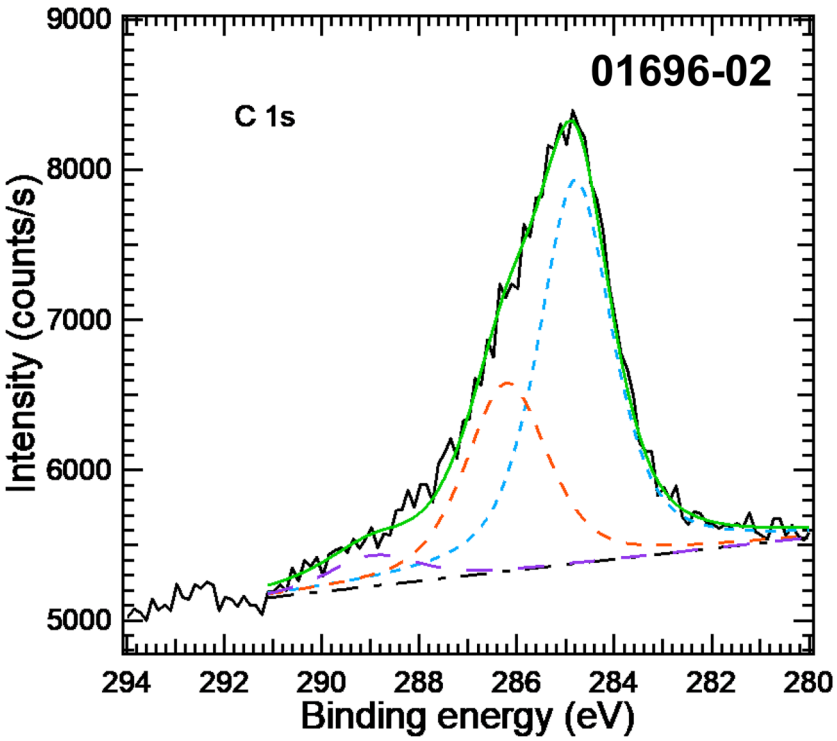

- **Accession #:** 01696-02
- **Host Material:** Fe_2O_3-WO_3
- **Technique:** XPS
- **Spectral Region:** C 1s

Instrument: Perkin-Elmer Physical Electronics, Inc. 5600ci
Excitation Source: Al K_α
Source Energy: 1486.6 eV
Source Strength: 250 W
Source Size: >25 × >25 mm^2
Analyzer Type: Spherical sector
Incident Angle: 9°
Emission Angle: 45°
Analyzer Pass Energy: 58.7 eV
Analyzer Resolution: 0.6 eV
Total Signal Accumulation Time: 137.0 s
Total Elapsed Time: 150.7 s
Number of Scans: 20
Effective Detector Width: 0.6 eV

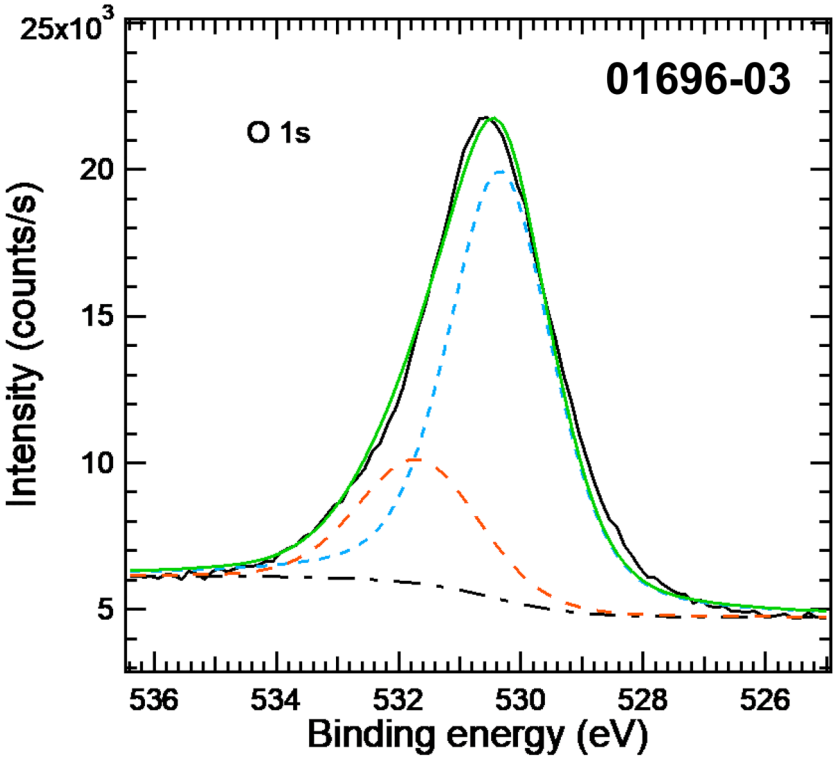

- **Accession #:** 01696-03
- **Host Material:** Fe_2O_3-WO_3
- **Technique:** XPS
- **Spectral Region:** O 1s

Instrument: Perkin-Elmer Physical Electronics, Inc. 5600ci
Excitation Source: Al K_α
Source Energy: 1486.6 eV
Source Strength: 250 W
Source Size: >25 × >25 mm^2
Analyzer Type: Spherical sector
Incident Angle: 9°
Emission Angle: 45°
Analyzer Pass Energy: 58.7 eV
Analyzer Resolution: 0.6 eV
Total Signal Accumulation Time: 121.0 s
Total Elapsed Time: 133.1 s
Number of Scans: 20
Effective Detector Width: 0.6 eV

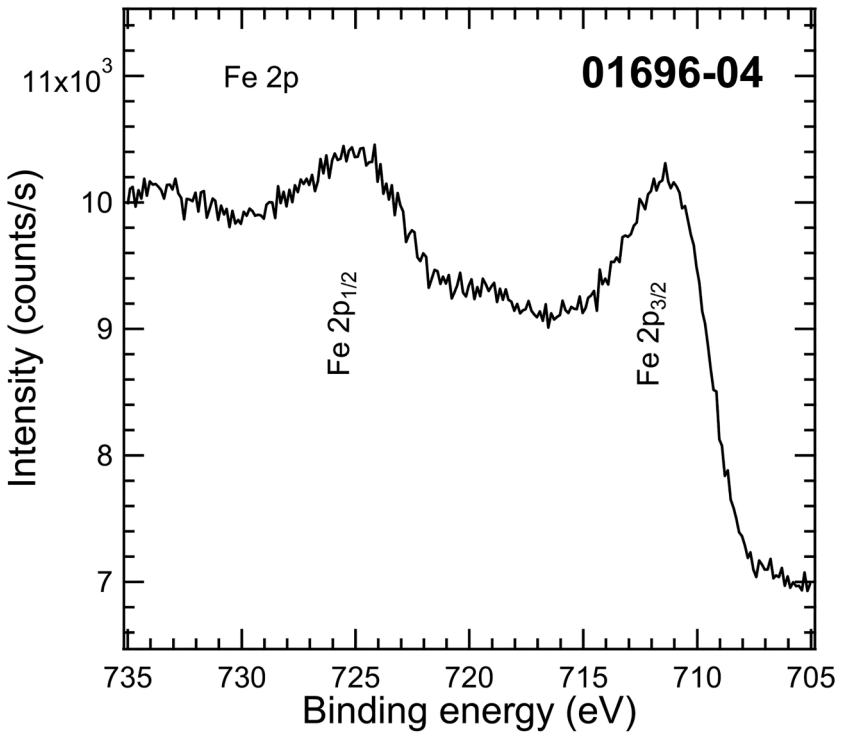

- **Accession #:** 01696-04
- **Host Material:** Fe_2O_3-WO_3
- **Technique:** XPS
- **Spectral Region:** Fe 2p

Instrument: Perkin-Elmer Physical Electronics, Inc. 5600ci
Excitation Source: Al K_α
Source Energy: 1486.6 eV
Source Strength: 250 W
Source Size: >25 × >25 mm^2
Analyzer Type: Spherical sector
Incident Angle: 9°
Emission Angle: 45°
Analyzer Pass Energy: 58.7 eV
Analyzer Resolution: 0.6 eV
Total Signal Accumulation Time: 802.5 s
Total Elapsed Time: 882.8 s
Number of Scans: 50
Effective Detector Width: 0.6 eV

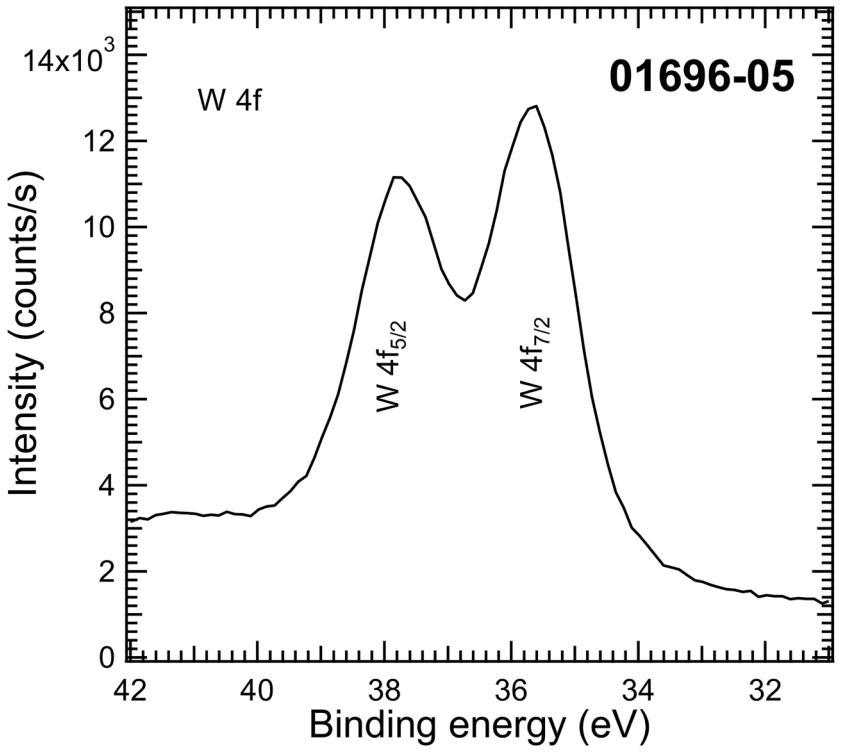

- **Accession #:** 01696-05
- **Host Material:** Fe_2O_3-WO_3
- **Technique:** XPS
- **Spectral Region:** W 4f

Instrument: Perkin-Elmer Physical Electronics, Inc. 5600ci
Excitation Source: Al K_α
Source Energy: 1486.6 eV
Source Strength: 250 W
Source Size: >25 × >25 mm^2
Analyzer Type: Spherical sector
Incident Angle: 9°
Emission Angle: 45°
Analyzer Pass Energy: 58.7 eV
Analyzer Resolution: 0.6 eV
Total Signal Accumulation Time: 225.8 s
Total Elapsed Time: 248.4 s
Number of Scans: 35
Effective Detector Width: 0.6 eV

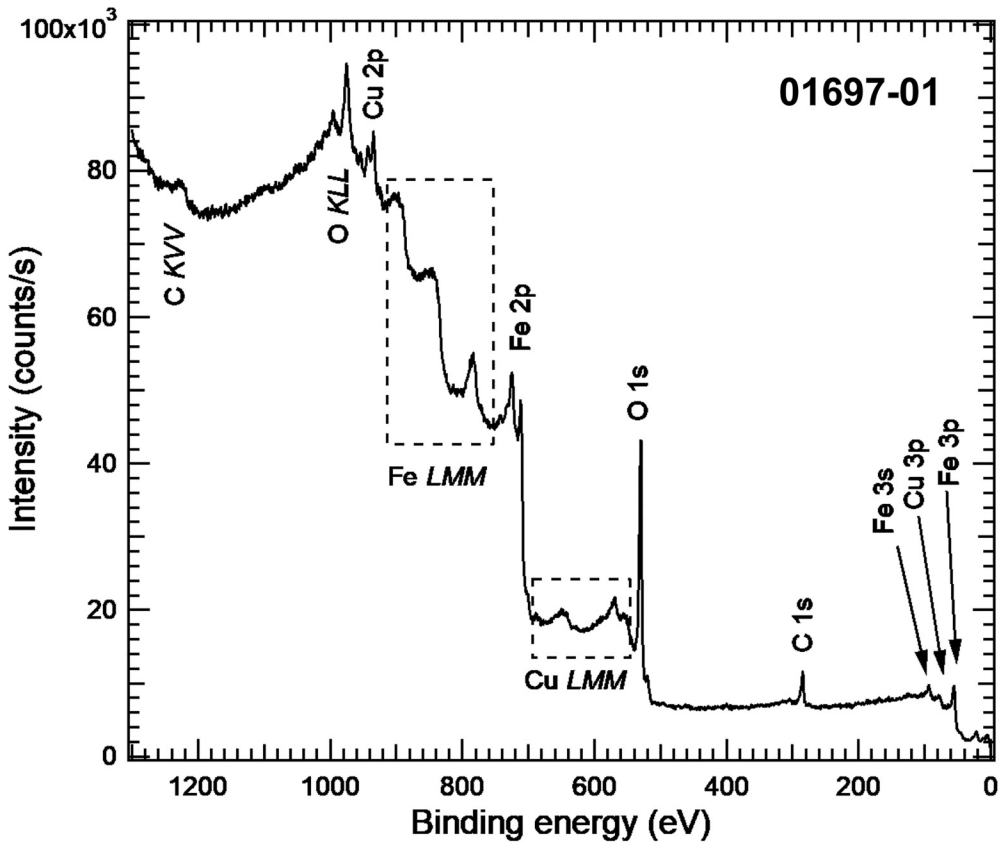

Accession #	01697-01
Host Material:	Fe_2O_3-CuO
Technique:	XPS
Spectral Region:	Survey
Instrument:	Perkin-Elmer Physical Electronics, Inc. 5600ci
Excitation Source:	Al K_α
Source Energy:	1486.6 eV
Source Strength:	250 W
Source Size:	>25 × >25 mm^2
Analyzer Type:	Spherical sector analyzer
Incident Angle:	9°
Emission Angle:	45°
Analyzer Pass Energy:	187.85 eV
Analyzer Resolution:	1.9 eV
Total Signal Accumulation Time:	650.4 s
Total Elapsed Time:	715.4 s
Number of Scans:	20
Effective Detector Width:	1.9 eV

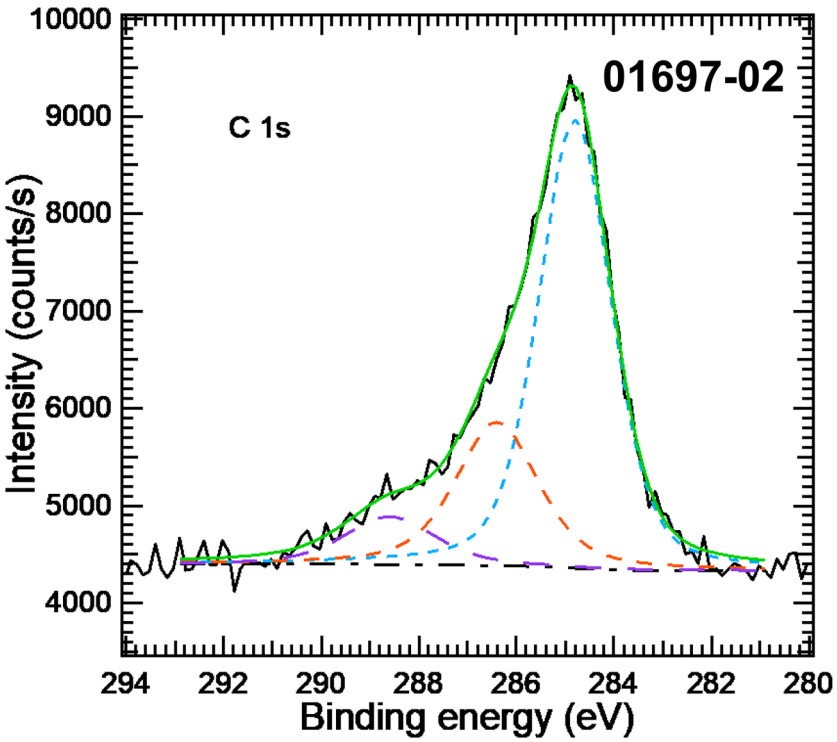

- **Accession #:** 01697-02
- **Host Material:** Fe_2O_3-CuO
- **Technique:** XPS
- **Spectral Region:** C 1s

Instrument: Perkin-Elmer Physical Electronics, Inc. 5600ci
Excitation Source: Al K_α
Source Energy: 1486.6 eV
Source Strength: 250 W
Source Size: >25 × >25 mm^2
Analyzer Type: Spherical sector
Incident Angle: 9°
Emission Angle: 45°
Analyzer Pass Energy: 58.7 eV
Analyzer Resolution: 0.6 eV
Total Signal Accumulation Time: 45.2 s
Total Elapsed Time: 49.7 s
Number of Scans: 8
Effective Detector Width: 0.6 eV

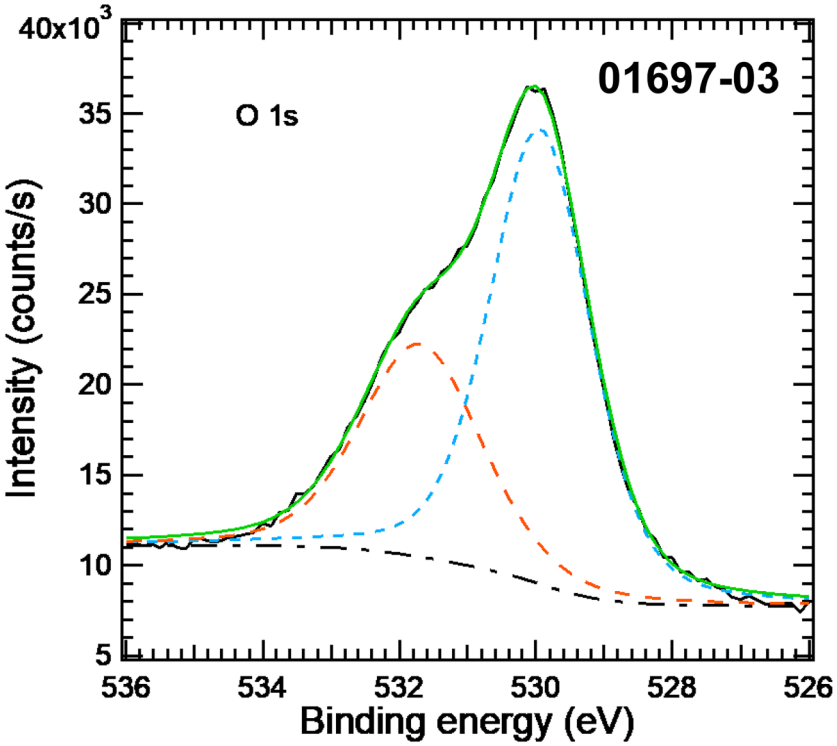

- **Accession #:** 01697-03
- **Host Material:** Fe_2O_3-CuO
- **Technique:** XPS
- **Spectral Region:** O 1s

Instrument: Perkin-Elmer Physical Electronics, Inc. 5600ci
Excitation Source: Al K_α
Source Energy: 1486.6 eV
Source Strength: 250 W
Source Size: >25 × >25 mm^2
Analyzer Type: Spherical sector
Incident Angle: 9°
Emission Angle: 45°
Analyzer Pass Energy: 58.7 eV
Analyzer Resolution: 0.6 eV
Total Signal Accumulation Time: 38.8 s
Total Elapsed Time: 42.7 s
Number of Scans: 8
Effective Detector Width: 0.6 eV

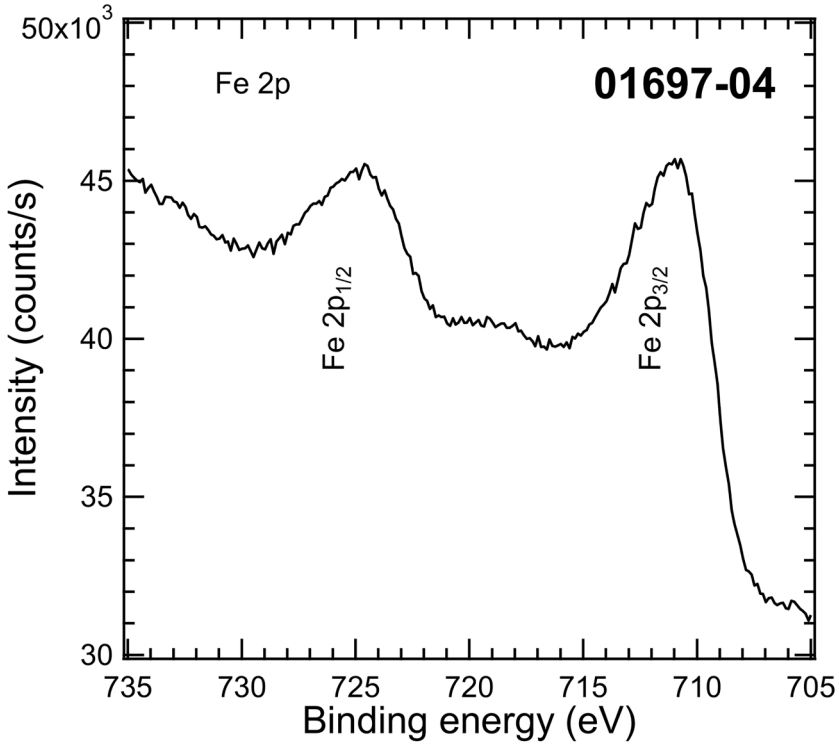

- **Accession #:** 01697-04
- **Host Material:** Fe_2O_3-CuO
- **Technique:** XPS
- **Spectral Region:** Fe 2p

Instrument: Perkin-Elmer Physical Electronics, Inc. 5600ci
Excitation Source: Al K_α
Source Energy: 1486.6 eV
Source Strength: 250 W
Source Size: >25 × >25 mm^2
Analyzer Type: Spherical sector
Incident Angle: 9°
Emission Angle: 45°
Analyzer Pass Energy: 58.7 eV
Analyzer Resolution: 0.6 eV
Total Signal Accumulation Time: 642.0 s
Total Elapsed Time: 706.2 s
Number of Scans: 40
Effective Detector Width: 0.6 eV

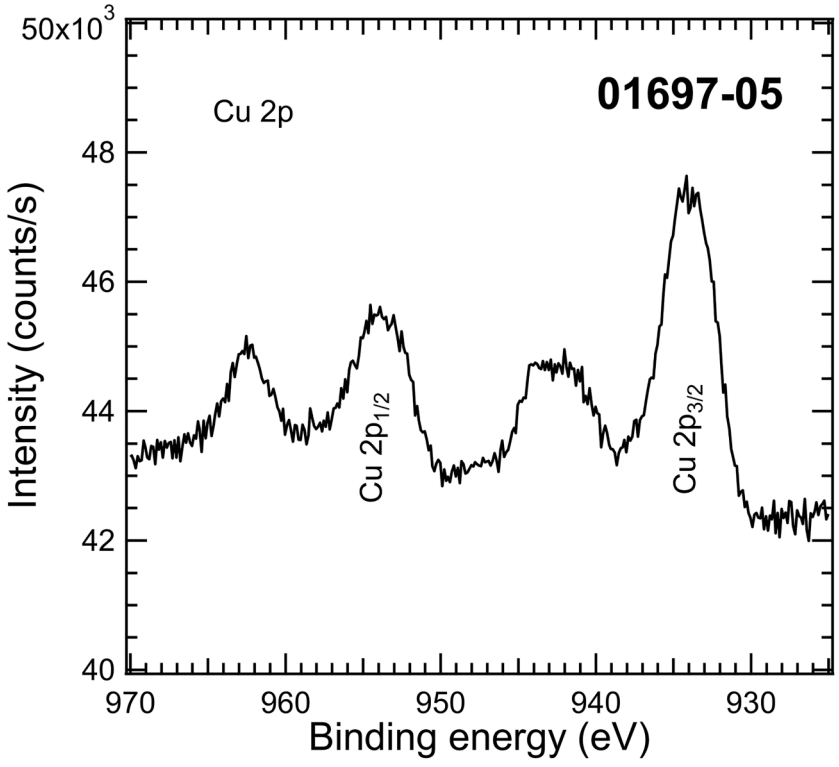

- **Accession #:** 01697-05
- **Host Material:** Fe_2O_3-CuO
- **Technique:** XPS
- **Spectral Region:** Cu 2p

Instrument: Perkin-Elmer Physical Electronics, Inc. 5600ci
Excitation Source: Al K_α
Source Energy: 1486.6 eV
Source Strength: 250 W
Source Size: >25 × >25 mm^2
Analyzer Type: Spherical sector
Incident Angle: 9°
Emission Angle: 45°
Analyzer Pass Energy: 58.7 eV
Analyzer Resolution: 0.6 eV
Total Signal Accumulation Time: 738.0 s
Total Elapsed Time: 811.8 s
Number of Scans: 40
Effective Detector Width: 0.6 eV

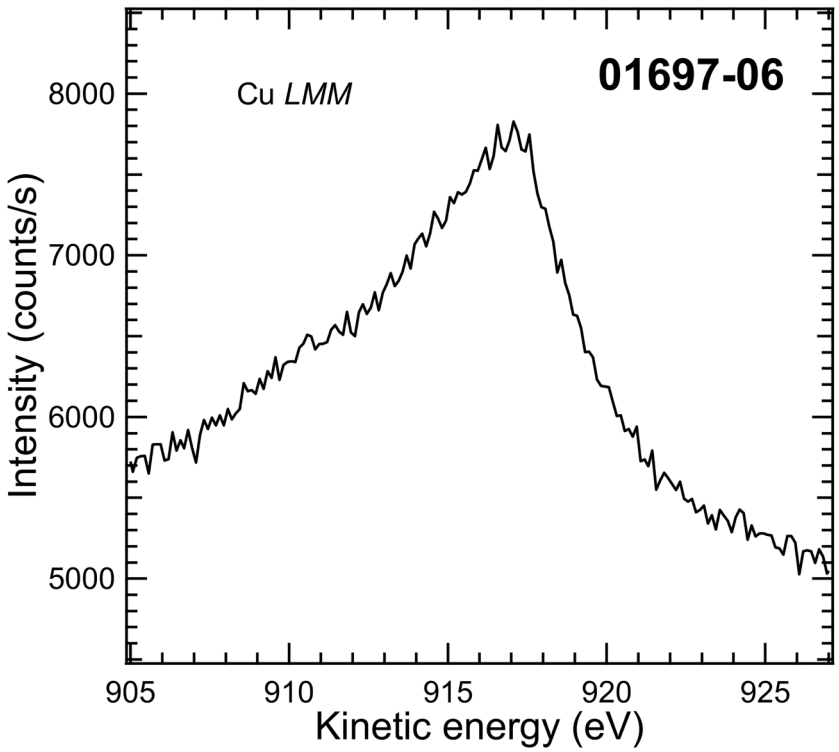

- **Accession #:** 01697-06
- **Host Material:** Fe_2O_3-CuO
- **Technique:** XE-AES
- **Spectral Region:** Cu LMM

Instrument: Perkin-Elmer Physical Electronics, Inc. 5600ci
Excitation Source: Al K_α
Source Energy: 1486.6 eV
Source Strength: 250 W
Source Size: >25 × >25 mm
Analyzer Type: Spherical sector
Incident Angle: 9°
Emission Angle: 45°
Analyzer Pass Energy: 58.7 eV
Analyzer Resolution: 0.6 eV
Total Signal Accumulation Time: 402.0 s
Total Elapsed Time: 442.2 s
Number of Scans: 40
Effective Detector Width: 0.6 eV